Time-Encoded Gamma-Ray Imaging Using a 3-D Position-Sensitive CdZnTe Detector Array

Steven T. Brown, David Goodman, Jiyang Chu, Bennett Williams, Martin R. Williamson, and Zhong He, *Senior Member, IEEE*

***Abstract*— The gamma-ray response of thick pixelated CdZnTe detectors varies spatially but is relatively constant as a function of time. Detector irregularities arise from flaws in the material, electrode fabrication, and gaps between the detectors in an array. These nonuniformities generate artifacts in coded aperture images that can obscure a source of interest. This article presents the theory, design, and demonstration of a 3-D CdZnTe-based time-encoded imager. Experimental results show the gamma-ray images of point-like and extended ^{57}Co and HEU-metal sources formed using a spatially nonuniform 3-D CdZnTe detector array and moving coded aperture mask. Image signal-to-noise ratio (SNR) for a point source was within 10% of its statistical limit at 250k counts.**

***Index Terms*— CdZnTe detectors, coded aperture imagers, detector arrays, gamma-ray detectors, radiation imaging, tomography, uranium.**

I. Introduction

TIME-ENCODED gamma-ray imaging was developed several decades ago to replace conventional collimator and pinhole imaging in nuclear medicine [1]–[3]. Based on imaging principles from X-ray astronomy [4]–[7], coded aperture imaging with time modulation provided higher detection efficiency, tomographic response, and smoothed nonuniform detector response. However, statistical gains were marginal due to the distributed nature of radiotracer uptake within the body [8], [9]. This shortcoming contributed to the eventual demise of the technology in the clinical setting.

Multiplexed pinhole imaging is statistically advantageous when an object of interest is hot relative to other emissions from within the field of view (FOV) or when there is significant noise due to an unmodulated background [10]. These conditions are common in the context of nuclear security, where coded apertures have more recently found utility [11]–[14]. Among these, time-modulated apertures have been used to address problems, such as orphan source search [15], [16]; stand-off fissile materials detection [17]; and high-resolution fast neutron imaging [18].

The motivating problem for this article is the so-called "black box" problem for nuclear security. In this scenario, nuclear materials concealed inside a container are characterized via passive, in-field measurements of leakage neutrons and gamma rays. Pixelated CdZnTe-based gamma-ray spectrometers are useful tools in this setting due to their high gamma-ray detection efficiency and good spectroscopic performance without cryogenic cooling. Human-portable array systems have shown better than 1% with analog [19] and about 0.6% FWHM with digital [20] electronic signal readouts at 662 keV. These systems can also Compton [21] and coded aperture [22] image; the latter is particularly useful for imaging X-rays and low-energy gamma rays emitted from special nuclear material.

However, the quality of coded aperture images from these systems is limited [23]. Aside from occasional flaws in electrode fabrication, thick CdZnTe is susceptible to material defects that have been shown to laterally deflect electric field lines on the order of 1 mm within a 10-mm drift distance [24]. This nonuniform behavior can complicate the detector spatial response and degrade the coded aperture image quality. On the other hand, CdZnTe response remains remarkably stable over time, even over long intervals [25], [26].

The goal of this article was to demonstrate that time-varying signals from 3-D CdZnTe can be used to form high-quality coded aperture images despite detector spatial defects. We used a simple linear model to show that coding artifacts are minimized by measuring the mask shadow as a function of time rather than space. We designed and built a time-encoded imager with a 2-D scanning mask and pixelated a CdZnTe detector array. Initial experimental results are reported for point-like and extended ^{57}Co sources as well as several extended U-metal objects. The presented work comes in large part from the thesis work of Brown [27].

II. Theory

Fig. 1 shows the coded aperture imaging using a thick position-sensitive CdZnTe detector. A far-field source of low-energy gamma rays casts the shadow of a coded aperture mask onto the detector. Each absorption in CdZnTe results in an electron cloud that drifts under bias toward a position-sensitive anode. The mean count distribution resembles the true shadow but is distorted due to the nonuniform detector response. Further detail on the detector irregularities observed in this article is provided in Section III-D.

Manuscript received December 28, 2018; accepted June 10, 2019. Date of publication November 12, 2019; date of current version February 13, 2020. This work was supported in part by the Department of Defense, Defense Threat Reduction Agency (3-D CZT Detectors and Readout Electronics) under Contract HDTRA1-15-C-0049, in part by the Department of Energy NA-22 Office (Image Reconstruction Algorithm Development) under Grant DE-NA002131, and in part by the National Science Foundation Graduate Student Research Fellowship under Grant DGE 0718128.

S. T. Brown, D. Goodman, J. Chu, B. Williams, and Z. He are with the Department of Nuclear Engineering and Radiological Sciences, University of Michigan, Ann Arbor, MI 48109 USA (e-mail: stbrow@umich.edu).

M. R. Williamson is with Consolidated Nuclear Security, LLC, Oak Ridge, TN USA.

Color versions of one or more of the figures in this article are available online at http://ieeexplore.ieee.org.

Digital Object Identifier 10.1109/TNS.2019.2953182

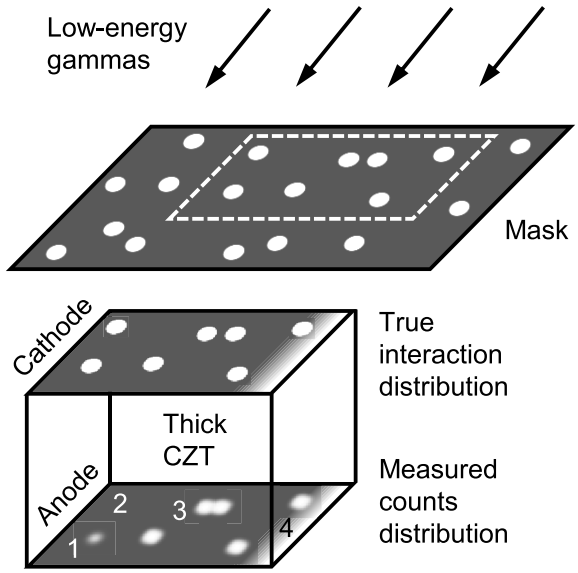

Fig. 1. Coded aperture imaging using thick pixelated CdZnTe. A low-energy, far-field source of gamma rays projects the shadow of a mask with an arbitrary pattern of holes onto the detector cathode surface, where photoelectric absorption takes place. Freed electrons drift from near the cathode, through the CdZnTe bulk material, and to the pixelated anode along the electric field lines. Nonuniform detector response is illustrated by: 1) an anode pixel with low sensitivity; 2) a dead anode pixel; 3) nonuniform electric field lines causing lateral charge drift; and 4) gamma rays incident on detector edge surface.

Time-encoded imaging is a type of coded aperture imaging that involves recording the mask's shadow as it moves over the detector. This may occur for a moving source, mask, detector, or any combination thereof. In this article, the mask moves, while the rest of the system is static. We reconstruct images from the time-varying count rate of each detector anode pixel and then sum over all anodes for better statistics. This technique was originally used for medical imaging by Koral *et al.* [1].

The following linear model describes the time-encoded imaging in a planar geometry with an imperfect multielement detector and scanning coded aperture mask. Notation is borrowed from the correlation model of Fenimore and Cannon [28]. The mask consists of a 2-D URA pattern of open and closed elements that are repeated at least once in both dimensions. A gamma-emitting object casts the mask's shadow onto the detector. During a measurement, the mask is cycled through its entire URA pattern, while each detector element records the count rate as a function of mask position. Due to the repeated mask pattern and detector parallax, the time-varying count rate measured by each detector element resembles the same signal but is circularly shifted according to the detector position. For simplicity, we assume that the object is fully coded by the mask, i.e., each emission point on the object generates a complete URA pattern of counts at each detector element.

The multielement detector consisting of K detector elements records a set of mask shadows represented by the 2-D functions $\boldsymbol{P_1}, \boldsymbol{P_2}, \ldots, \boldsymbol{P_K}$ (deadtime-corrected count rates as a function of mask position). The detector used in this article has a stable response over time and a directionally dependent sensitivity that varies by detector element, as described in Section III-D. If we represent the kth intrinsic detector efficiency by ϵ_k (expected counts per incident gamma), its solid angle by $\boldsymbol{\Omega_k}$ (detector solid angle versus source position), aperture function by $\boldsymbol{A_k}$ (URA pattern of transmission probabilities), and emitting object by $\boldsymbol{O}$ (emission rate per unit solid angle versus source position), then the mean shadow recorded by the kth detector is

$$\boldsymbol{P_k} = \epsilon_k \boldsymbol{A_k} * (\boldsymbol{\Omega_k} \circ \boldsymbol{O}) + \boldsymbol{N_k} \tag{1}$$

where $*$ is the periodic correlation operator, $\circ$ is the Hadamard (element-wise) product, and $\boldsymbol{N_k}$ is additive noise from unmodulated background sources. Gammas from the object that transmit through closed elements of the mask contribute a constant count rate or dc offset to $\boldsymbol{P_k}$. This linear model ignores collimation effects from a thick mask.

The image from the kth detector element can be reconstructed via periodic correlation of its measured shadow with the corresponding decoding array $\boldsymbol{G_k}$ such that $\boldsymbol{G_k} * \boldsymbol{A_k} = \boldsymbol{\delta}$, where $\boldsymbol{\delta}$ is Dirac's delta function. The decoded image summed over all detector elements is then

$$\hat{\boldsymbol{O}} = \sum_k \boldsymbol{G_k} * \boldsymbol{P_k} = \boldsymbol{O} \circ \sum_k \epsilon_k \boldsymbol{\Omega_k} + \sum_k \boldsymbol{G_k} * \boldsymbol{N_k}. \tag{2}$$

Neglecting the background noise term, the object estimate resembles the true object modulated by detector-averaged directional sensitivity, which tends to vary smoothly and predictably over the FOV. Furthermore, if $\boldsymbol{N_k}$ is nonzero but static, then the background term becomes an easily removable dc offset in the reconstructed image.

Conventional or static-mask imagers measure the mask shadow as a function of position rather than time, so the recorded shadow is modulated not only by the mask but also by nonuniform detector efficiencies and solid angles. The mask–antimask technique, which removes additive noise in coded aperture images, can reduce but not exactly cancel this additional modulation [29], [30]. On the other hand, Grindlay and Hong [31] have shown that multiplicative errors such as these are exactly removed by scanning the mask through its entire cycle. This is consistent with (1) and (2), which indicate that each detector element acts as a stand-alone imager that is independent of the varied response of its neighbors. A single detector element may also record coded patterns of arbitrary rank, given that there is enough time to move the mask through its cycle. This feature of time-encoded imaging motivated the design of the high-rank mask used in this article.

III. Time-Encoded Imager Design

A. Method for Time Modulation

Our objective was to design a time-encoded imager that would resolve a large number of resolution elements with minimal image artifacts. Ideally, the mask would be entirely adaptable. While there has been progress made in the way of adaptive liquid mask collimators [32], the complex design was not feasible, given our desire for many mask elements. Early work in time-encoded imaging utilized a 1-D uniformly redundant array arranged in rows and shifted through the imager FOV in one direction [1]. While this method is mechanically

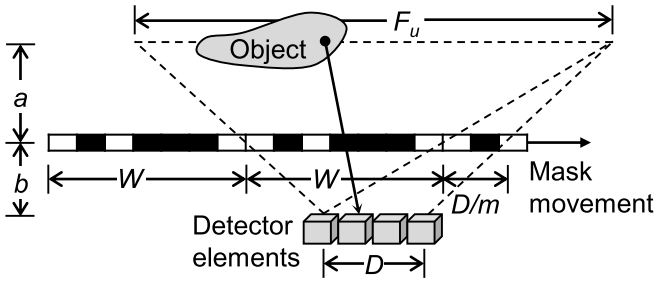

Fig. 2. 1-D depiction of time-encoding scheme used in this article.

simple, it requires a mask of size $\sqrt{N} \times N$, where N is the total number of elements in the basic code. Each row of the mask consists of the same length-N pattern but cyclically shifted by $\sqrt{N}$ elements so that horizontal linear motion always results in a cyclic shift of the same basic pattern within the FOV. Hence, the mask can become quite large for large N.

The approach used here was similar to the scanning coded aperture technique proposed by Grindlay and Hong [31] for X-ray astronomy. Rather than scaning the sky, our approach was to move the mask in an otherwise stationary system to measure the objects in the near field. Fig. 2 shows a 1-D illustration of our implementation. In this diagram, a single cycle of the mask pattern has $N = 7$ elements with total width $W = Np$, where p is the pitch of the coded aperture mask elements. The fully coded FOV of each mask element overlaps at the object plane to form a uniformly sampled FOV of length $F_u = (1 + a/b)W$, which is subtended by a full mask cycle. Note that there are extra mask elements at the right to account for the detector extent; the mask has added length D/m, where D is the total detector extent and $m = 1 + b/a$ is the mask shadow magnification at the detector plane. The added mask length causes additional aliasing but results in shorter measurement times compared with the original mask moved further to compensate. The region to the right and left of the fully coded FOV is analogous to the partially coded FOV in conventional coded aperture imaging.

During a measurement, the mask of Fig. 2 is shifted one element at a time toward the right until an entire pattern cycle has been traversed. Drawing a line of sight between any detector element and source location, one can see that particles along that trajectory are modulated in time by the coded aperture pattern as the mask is shifted. In this setup, each detector element in the array records a cyclically shifted, or phase-shifted, version of the same time-varying signal. The 2-D arrangement is similar to that of Fig. 2, except that the mask moves along a boustrophedonical route rather than in one direction, as shown in Fig. 3(a). This approach requires a number of mask elements of order $\sqrt{N} \times \sqrt{N}$, enabling the use of reasonably sized masks for large N patterns at the cost of greater mechanical complexity.

B. "Mira" Mask Positioning System

A programmable mask positioning system named Mira was designed to provide time modulation. Fig. 3(a) shows the system with a single plane of Polaris SP. Throughout the following experimental work, all nine CdZnTe crystals had cathodes facing the mask and were fixed to an adjustable stage to control the detector-to-mask distance. Vertical and horizontal ball screws are each connected to a stepper motor wired to a driver and controlled using a common Arduino Uno board. The two degrees of freedom provided by the perpendicular ball screws allow for accurate (x, y) positioning of a coded aperture mask. Data were recorded by a laptop from both Mira and Polaris SP and their timing was synchronized to 1-ms precision using the laptop's system clock.

C. Coded Aperture Mask

The coded aperture mask is made up of several identical stacked sheets of 0.25-mm-thick W metal. Total mask thickness is therefore adjustable depending on the number of sheets used. The pattern of holes was fabricated by Tech Etch, Inc., of Plymouth, MA, USA. Fig. 3(b) shows the photographs of a single mask layer and a close-up of eight stacked layers to show detail. The square pattern is an order-79 MURA repeated about 2.5 times in 2-D for a total of 200×200 1.4-mm-pitch elements. The number of elements was chosen such that each W sheet, including a 6-mm-wide border for positioning, was within the 12 in $\times$ 12 in footprint limited by the fabrication process. Since the MURA pattern is not self-supporting, there are 0.424-mm-wide strips of W metal connecting the neighboring corners. It is about 50% open and arranged so that the mask is nearly antisymmetric upon 90° rotation, enabling mask–antimask correction [33].

Although this correction may be used to remove unmodulated background in the time domain, it was not used here. Aside from the fact that the steady the background rates experienced in this article primarily added a negligible dc component to the images, time-varying background must fluctuate in the same way during both mask and antimask measurements for it to cancel. For example, a moving mask apparatus might scatter particles toward the detector and create a time-varying nuisance signal that is identical regardless of the mask used. In that case, the mask–antimask method would remove the nuisance signal. Although it is common for the background to vary in the same way spatially from one measurement to the next, the time analog is not as common. Future studies may be performed to investigate time-varying background removal in special cases.

D. Polaris SP Detector Array

The Polaris SP detector system consists of two separate 3×3 arrays of 20 mm $\times$ 20 mm $\times$ 15 mm $Cd_{0.9}Zn_{0.1}Te$ with 2-mm gaps between the detectors. Each detector has 11×11 pixelated anodes with 1.72-mm pitch affixed to one square side with a planar cathode on the opposite side. The small pixel effect provides the 3-D position sensitivity used for spectroscopic calibration of the device [19].

For coded aperture imaging, gamma-ray interaction positions were integrated along the direction between the cathode and anode planes, i.e., the array was treated as a 2-D position-sensitive detector plane for imaging. Signals from each detector channel were read out using an analog ASIC [34]. Polaris SP is similar in terms of spectroscopic

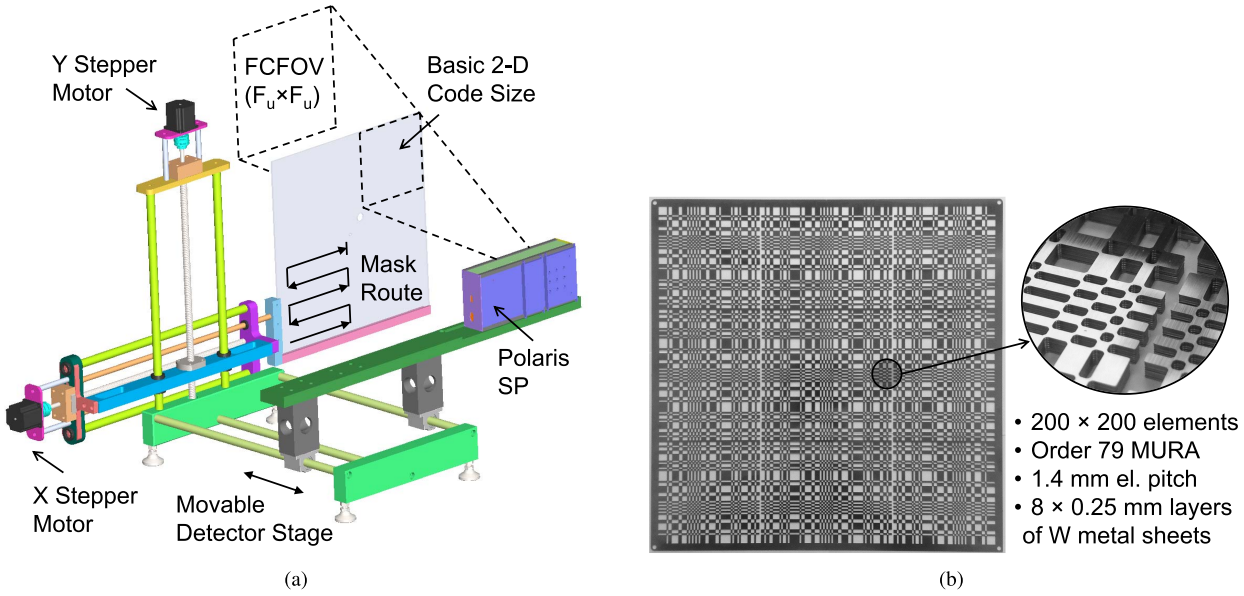

Fig. 3. (a) 3-D rendering of the mask positioning system, Mira, with Polaris SP detector. (b) Photograph of the coded aperture mask. Inset image is a close-up of eight W-metal sheets stacked to form a 2-mm-thick mask.

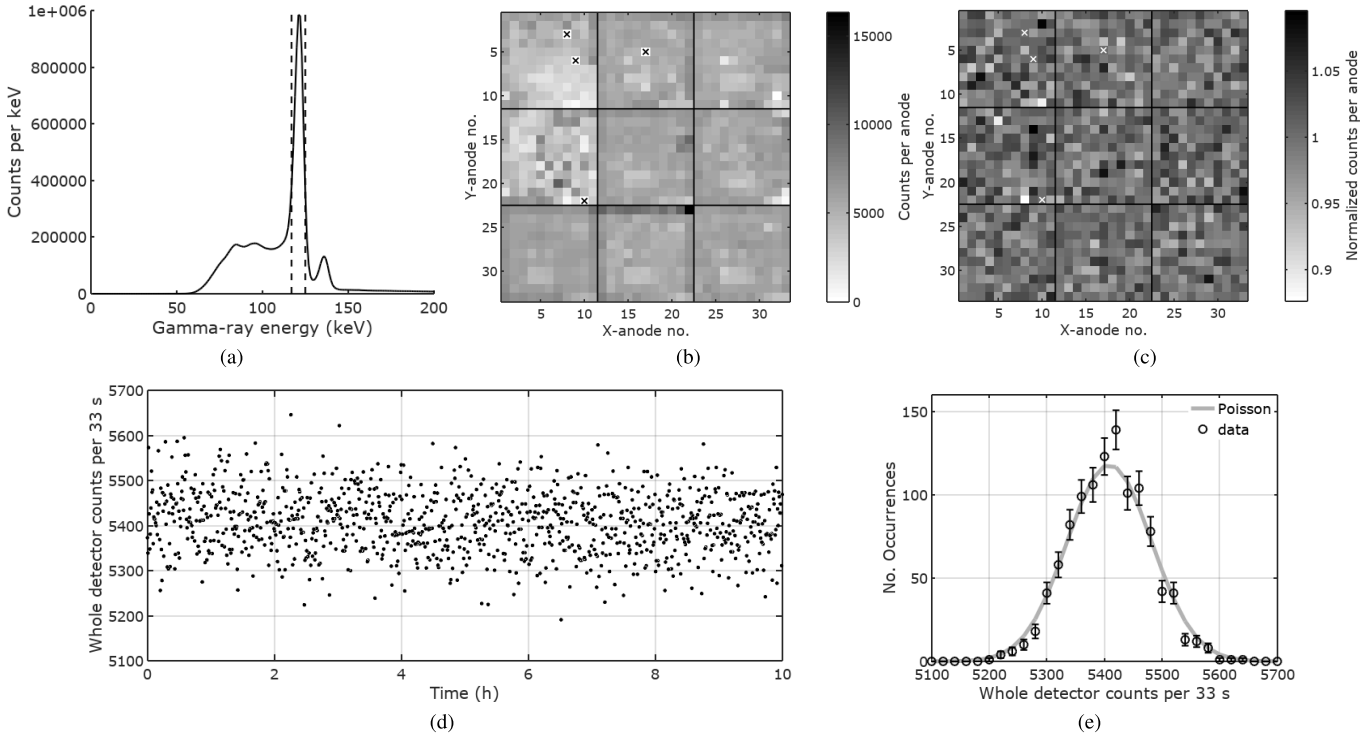

Fig. 4. Distribution of counts from a 10-h flat-field ^{57}Co irradiation of Polaris SP. (a) Total gamma-ray spectrum with energy window bounded by the dashed line. (b) Spatial count map binned by 33^2 anodes. Black solid lines: detector crystal boundaries. ×: dead detector pixels. (c) Spatial count map measured during last 5-h flat fielded with counts from the first 5 h. (d) Counts for 33-s time bins. (e) Histogram of data from (d) compared to a Poisson distribution with the same mean.

performance and construction to previous iterations of array systems [19].

To characterize Polaris SP's response, a single plane was uniformly illuminated using a far-field ^{57}Co point source for 10-h overnight. Total count rate was about 700 cps. Counts within the 122-keV energy window of Fig. 4(a) were binned by the detector pixel and plotted in Fig. 4(b). In total, 5.9×10^6 single-pixel interactions were recorded within the energy window from 117 to 125 keV or 5409 counts per pixel on average. If the number of counts per pixel was independent and Poisson distributed, their relative standard deviation would be 1.4%. However, due to the systematic variations in detector response, the relative standard deviation was 26%.

Although no correction was applied in this article, some of the systematics seen in Fig. 4(b) are not inherent. For example, the top-left and center-left detectors have systematically fewer counts due to the miscalibrated gain. Edge pixels have a slightly larger effective area than the inner 9×9, as evidenced

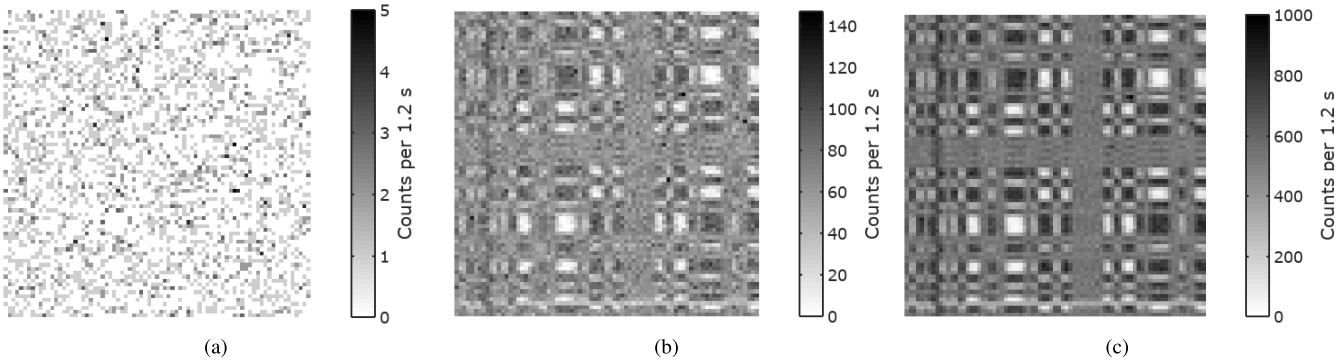

(a) (b) (c)

Fig. 5. Time-binned patterns of 122-keV gamma-ray interactions measured using (a) single anode pixel, (b) single detector, and (c) all nine detectors.

by their elevation in counts in Fig. 4(b). Not only do those pixels record more counts on average, but also because of their location at the crystal edge, their effective solid angle relative to the source changes significantly as a function of source direction. A similar measurement to that of Fig. 4(b) except with the source 45° from normal showed that counts at the outer edges of the array increased fourfold and counts on the inner edges of the 3×3 detectors changed by $\pm 50\%$. Because of its strong dependence on source direction and energy, Polaris SP's response cannot be flattened using a conventional flood correction.

Polaris SP's time response, on the other hand, was relatively uniform. Fig. 4(d) shows the counts tallied in 33^2 time bins during the 10-h measurement, the same total bins used in Fig. 4(b). The distribution of time-binned counts plotted in Fig. 4(d) had 1.3% relative standard deviation and was not significantly different from a Poisson distribution with the same mean, $\chi^2(1, 18) = 24.5$ and $p = .14$. No significant deviation from Poisson was observed for the same data binned by 1 s. However, a data buffer issue was observed at count rates greater than roughly 1000 cps, introducing spikes in count rate discussed in Section IV-A2.

Fig. 4(c) shows the count map for the last 5 h of measurement, flat fielded (normalized) by the first 5 h. The systematics seen in Fig. 4(c) were reduced from 26% to 2.8% standard deviation. This suggests that Polaris SP has a spatially varying response that remains relatively static over the period of several hours, which is the measurement duration we are interested in.

IV. Experimental Results

Two sets of time-encoded gamma-ray imaging measurements were taken using Polaris SP and the mask positioning system. Image quality was initially characterized using several ^{57}Co sources at the University of Michigan, and then uranium metal objects were measured at the Y-12 Nuclear Detection and Sensor Testing Center (NDSTC). All images presented here were reconstructed via periodic correlation of the measured time-binned pattern with an order-79 MURA decoding array. Unless stated otherwise, reconstructed images are plotted with black- and white-color scale spanning the minimum and maximum values of the image.

By design of the mask, each detector voxel recorded the same time-varying signal but with different phases. For image reconstruction at some distance from the mask, signals were cyclically shifted according to the voxel position and mask shadow size such that their phases aligned prior to summation. In an actual black box scenario, the object distance is unknown, and therefore, several tomographic slices would be reconstructed to form a 3-D image.

Unless stated otherwise, the total measured pattern was binned on a 79×79 grid before correlation with the mask's decoding pattern. The mask dwelled at a discrete set of 79×79 positions during measurement; data recorded as the mask traveled between those positions was ignored for simplicity. Measurement times are reported here without mask travel time, which took an additional 30 min for all 79^2 movements.

A. ^{57}Co Gamma-Ray Sources

1) Check Source, Close to Mask: The 53 μCi ^{57}Co check source had a nominal active diameter of 5 mm centered within a 1-in-diameter plastic disk. The disk was placed 1 cm from the mask, which was 28 cm from the cathode surfaces of Polaris SP; 1-mm-thick W metal was used for the mask, which absorbs about 99% of incident 122-keV gamma rays. The measurement was taken for about 2 h at 1365 cps. A 1.2-s dwell time was used at each of the 79^2 mask positions during the measurement. The same energy window of Fig. 4(a) was used with a similar measured spectrum and minimal background.

Fig. 5 shows the time-binned patterns measured by a single anode, 121 anodes belonging to a single detector, and all 1089 anodes in the array. To avoid systematic error from detector deadtime, a nonparalyzable deadtime correction was applied to each time bin. Fig. 6 shows the deadtime-corrected images reconstructed via correlation of each measured pattern with the decoding array. Although the measured pattern from a single anode shown in Fig. 5(a) is not discernible, the correlation reconstruction was able to recover the source's location in Fig. 6(a), albeit with substantial statistical noise. The images using the detector and array appear nearly uniform, with a faint cross-shaped artifact centered on the source location and spanning the entire image. The root cause of this artifact is not yet understood.

The image SNRs of Fig. 6(a)–(c), defined here sum of source pixels divided by the rms deviation of the non-source pixels, are 51, 457, and 996, respectively. Because the source was very near the mask, the overall count rate

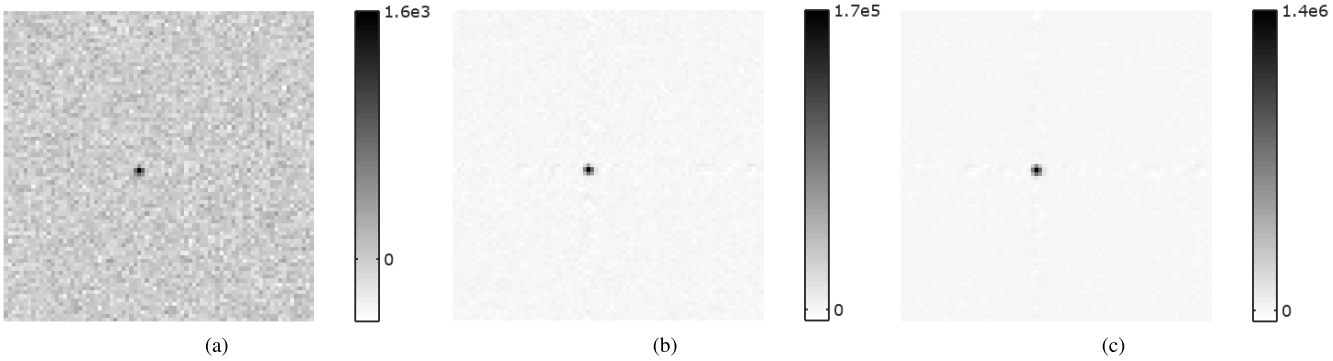

Fig. 6. Deadtime corrected images of a ^{57}Co check source using measured patterns of (a) Fig. 5(a) (SNR = 51), (b) Fig. 5(b) (SNR = 457), and (c) Fig. 5(c) (SNR = 996).

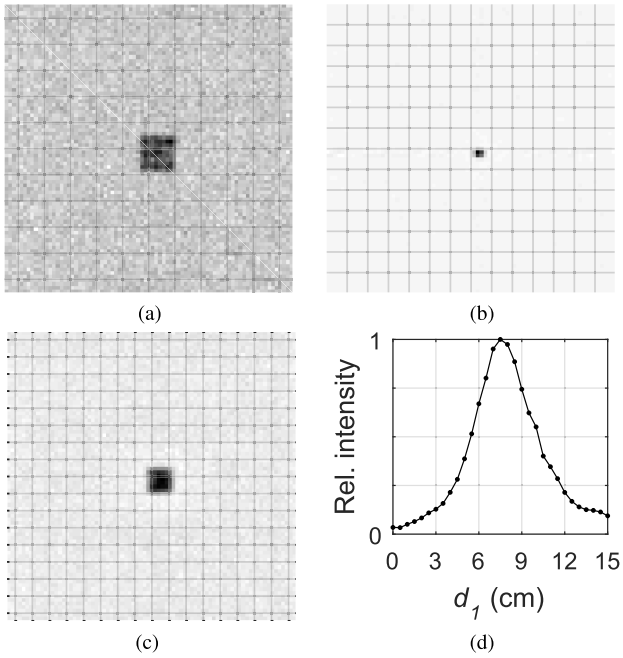

Fig. 7. 3-D reconstruction of a ^{57}Co check source located 7.5 cm from the mask. (a)–(c) Frontal image slices for several mask-to-object distances. (d) Reconstructed intensity as a function of mask-to-object distance through the maximum intensity pixel. Image grid lines have 1-cm pitch. (a) a= 0 cm (b) a= 7.5 cm (c) a= 15 cm.

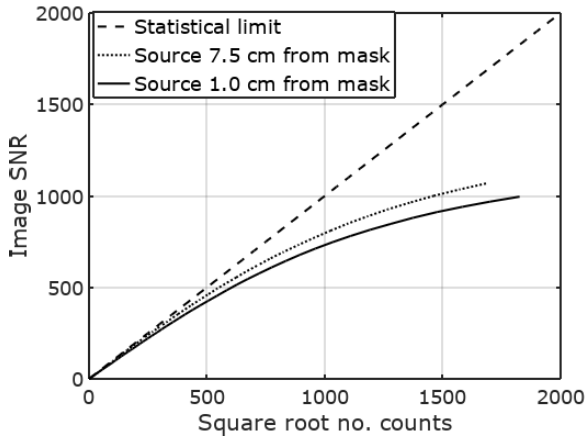

Fig. 8. Image SNR as a function of imaged counts, proportional on average to the number of detector anodes included during reconstruction, for the data of Figs. 5 and 6.

fluctuated significantly during the measurement; without deadtime correction, these SNRs were reduced by about 30%.

2) Check Source, Away From Mask: The same ^{57}Co check source was then placed 7.5 cm from the mask, while the mask-to-detector distance remained 28 cm. The purpose was to observe the smooth 3-D focusing effect from parallax. The measurement time was again 2 h with an average count rate of 1190 cps. The same energy window of Fig. 4(a) was used with a similar measured spectrum and minimal background.

Fig. 7(a)–(c) shows the images reconstructed at three different object planes away from the mask. Separate hotspots contributed by each of the 3×3 detectors are discernible at the mask plane in Fig. 7(a). The absence of additional artifacts in the two out-of-focus planes suggests that each detector acts as an independent imager. Fig. 7(d) shows a plot of reconstructed intensity as a function of depth through the maximum intensity pixel, showing the peak intensity around 7.5 cm with 5-cm FWHM.

The SNR of the deadtime-corrected image at 7.5 cm is plotted as a function of counts in Fig. 8, where the endpoint SNR is 1069. In contrast to the 1-cm-away image, forgoing a deadtime correction for this image only caused a 4% reduction in SNR because the source was positioned farther from the mask. Lower magnification also meant that the alignment of each anode signal's phase smoothed detector-wide aberrations in count rate, including the spikes in count rate from data buffering. Fig. 9 shows that the alignment process eliminated these spikes, where Fig. 9(a) and (b) shows the patterns used to reconstruct the images of Fig. 7(a) and (b), respectively.

Fig. 8 shows that image SNR for this measurement was about 10% greater than the 1-cm-away measurement. Both sources were near the FOV center, so the difference can be mainly attributed to the smoothing effect shown in Fig. 9. At the 7.5-cm source distance, the shadow of one element took about 11 s to traverse the detector plane, so fluctuations across multiple anodes were spread out over that time interval. At the 1-cm source distance, the effect was diminished since the smoothing occurred over just 2 s.

3) Flexible Marker, Coiled: An extended object was imaged next. The source was 85 μCi ^{57}Co in solution within a 50-cm-long plastic tube. The inner diameter of the tube containing the solution was 0.8 mm with an outer diameter

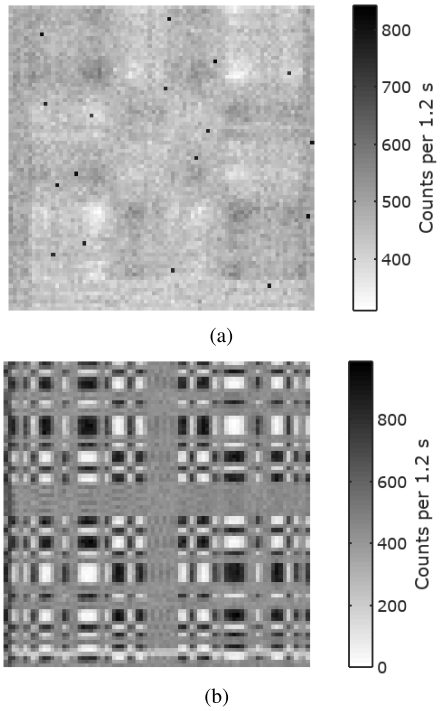

Fig. 9. (a) 121-keV count rate versus time summed over the whole detector during the 7.5-cm-away point source measurement. Black pixels correspond to count rate spikes from a data buffer issue. (b) Same data from (a) but with anode signal phases aligned according to source distance.

2.4 mm. The source was coiled in a circular shape and placed within the 12-cm diameter CD case pictured in Fig. 10.

The 50-cm tube length exceeded the circumference of the circle, so the coiled tube overlapped itself. At the right side of the image, the tube was deliberately pressed up against itself such that its edges were touching. The tube then gradually diverged away from this position to provide a range of tube separations. The case was positioned parallel to the mask and 2 cm from its surface. The mask-to-detector plane distance was again 28 cm. The source was measured for 8.5 h at 1720 cps. Counts were binned in time 10× more finely in 2-D (790×790 bins) prior to correlation to allow for more precise interaction position information to be used.

Unfortunate placement of the source meant it was actually slightly larger than the FOV at the object plane, which was 11.8 cm on a side. Therefore, gamma rays from the vertical and horizontal edges of the tube were encoded with the same time-varying pattern, making their respective signals ambiguous. The reconstructed image is shown in Fig. 10(b) with a color scale spanning the minimum and maximum image pixel values outside of the overlapping parts of the coil. Despite the aliasing, the tube pinch point at the right side of the image is well separated. The center-to-center tube distance at these locations was 2.4 mm, so the separation of their inner regions containing ^{57}Co was about 1.6 mm. System spatial resolution was expected to be about 1.5 mm, given the detector resolution and mask element size.

B. U-Metal Objects

1) Highly Enriched U-Metal Disks: A pair of 3-cm-diameter, 3-mm-thick U-metal disks were measured at the Y-12 NDSTC. The disks were positioned with circular

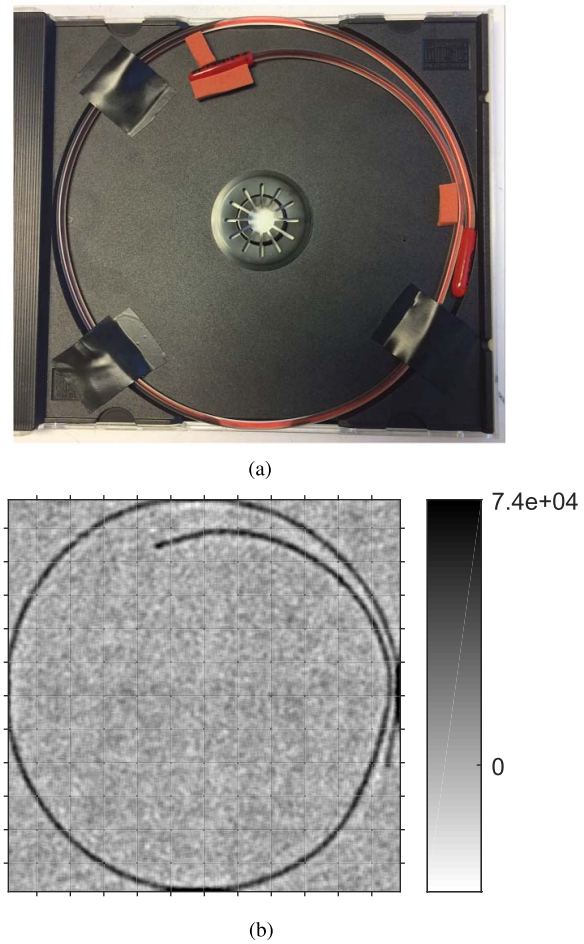

Fig. 10. (a) Coiled tube containing red ^{57}Co solution inside a CD case. (b) Reconstructed image. Image grid lines have 1-cm pitch.

surfaces facing the mask, one 54% and the other 70% ^{235}U. The 54%-enriched disk was positioned 3.6 cm away from the mask, while the 70% disk was 6.9 cm away. The mask was 2 mm thick and positioned 28 cm from the detector. Two 1.5-h measurements were acquired and summed. The count rate was 670 cps with measured energy spectrum plotted in Fig. 11(a). The spectrum was dominated by U X-ray and ^{235}U gamma-ray lines up to 205 keV.

All single-pixel events below 215 keV were used for the images of Fig. 11(b) and (c). Note that the outline of each disk is sharpest at the plane where it was actually positioned. With knowledge of the experimental setup, we determined that the difference in intensity between the disks is mainly due to their difference in enrichment. However, accurate enrichment estimates require minimal image artifacts; only then may spectral-imaging deconvolution techniques, such as that employed by Ziock *et al.* [35], be used reliably. The images indeed have some subtle structure in their backdrop, which may be the result of the same artifacts observed in Fig. 6(b) and (c). Room scatter may also have contributed since it was partially modulated by the mask outside the fully coded FOV.

2) Depleted and Natural U-Metal Disks: An overnight measurement was taken for 14.5 h using NU- and DU-metal disks. The setup was similar to the previous measurement,

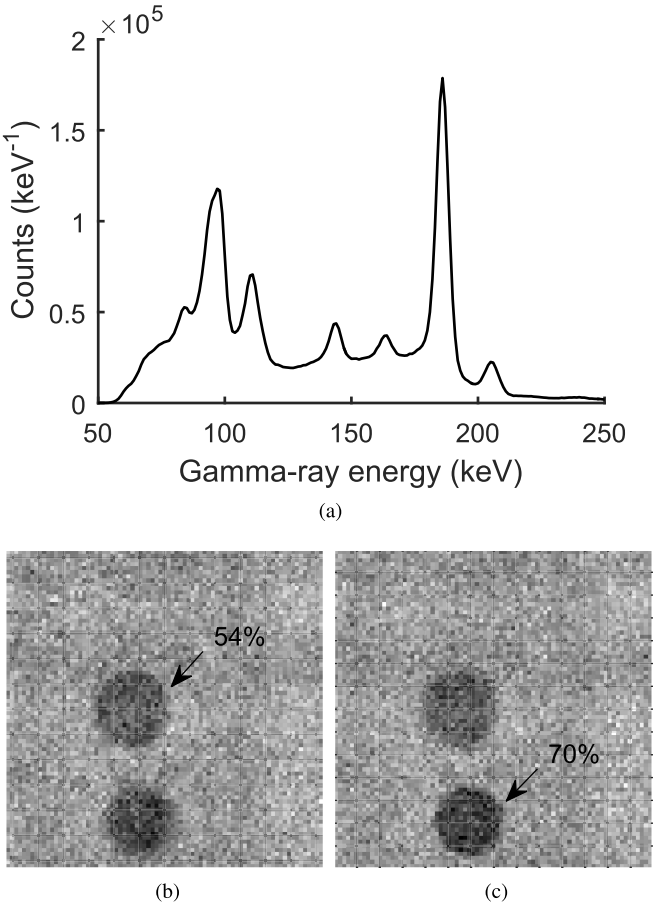

Fig. 11. (a) Measured HEU spectrum. (b) and (c) Reconstructed images of two HEU disks at their respective mask-to-object distances, $d_1 = 3.6$ cm and $d_1 = 6.9$ cm, respectively. The enrichment of each disk is indicated for the image in which it is properly focused. Image grid lines have a 1-cm pitch.

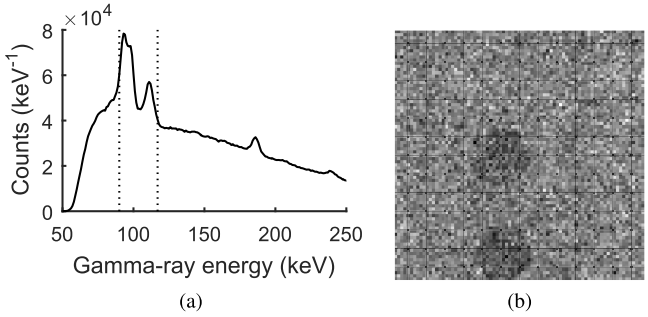

Fig. 12. (a) Measured low-enriched U-metal gamma-ray spectrum. (b) Reconstructed image of the DU- (top) and NU-metal (bottom) disks. Image grid lines have a 1-cm pitch.

except that the DU disk was 4.3 cm away from the mask and the NU disk was 7.1 cm away. The low enrichment of the sample meant that ^{235}U lines were not prominent, so the K X-rays near 95 and 111 keV were used for imaging. The total count rate was 215 cps.

Fig. 12(a) shows the measured spectrum and energy window. Low count rate and prominent background contributed to the statistical noise that dominates the image of Fig. 12(b), reconstructed at 5.1 cm from the mask. Since the relatively strong background rate was constant as a function of time, the two disks are still discernible among the noise.

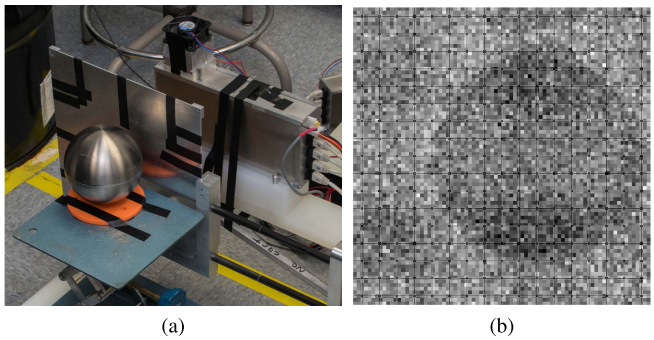

Fig. 13. (a) Photograph of RSTD and time-encoded imager. (b) Reconstructed image. Image grid lines have 1-cm pitch.

3) Radiation Signature Training Device (RSTD): The spherical RSTD consists of a 12.6-cm-outer diameter shell of Al-HEU metal alloy with DU-metal core. Spectroscopically, it mimics a larger quantity of HEU metal. The device is pictured along with Polaris SP and mask in Fig. 13(a). The RSTD was placed in the near field with its front edge 1.7 cm from the mask, while the mask-to-detector distance was 14.8 cm. The objective was to determine whether the hollow center of the Al-HEU alloy shell was discernible from the time-coded image of ^{235}U gamma-ray emissions, closer proximity-enhanced parallax. The measured count rate was high, about 1900 cps, resulting in nearly 80% deadtime. No deadtime correction was used due to the large extent of the source; the total count rate was roughly constant throughout. All counts below 215 keV from 4.5-h measurement were used to form the image.

The reconstructed image at the centerline of the object (8 cm from the mask) is presented in Fig. 13(b). The object subtended a large fraction of the FOV due to its proximity, so its intensity was spread across many image pixels. A coded aperture mask of lower open fraction would have been statistically favorable to the MURA in this case. Nevertheless, the distribution of intensity in Fig. 13(b) does appear to outline a circular shape of the correct size. It is difficult to draw any firm conclusion regarding its hollow structure due to the combination of statistical fluctuations and systematic artifacts exaggerated by the very large extent of the object.

V. Conclusion

We designed, built, and tested a prototype time-modulated coded aperture imager with a thick pixelated CdZnTe detector array. The design was based on the well-known principles of coded aperture imaging, which have shown the advantage of time modulation for detectors with spatially nonuniform response. Although Polaris SP was shown to be stable over time at low count rates, it was subject to temporal fluctuations during these measurements, including a data buffer issue that caused detector-wide count rate spikes during some measurements.

Nevertheless, ^{57}Co point source data showed that SNR reached 84% of its statistical limit at 250k counts for sources very near the mask (mask magnification 29) and increased to 91% when the magnification was reduced to 5. This improvement was attributed to the smoothing of spurious fluctuations

in count rate across multiple anodes. Data from the detector anodes were subject to these fluctuations simultaneously but measured the mask's shadow out of phase, a feature of the mask, and its movement routine.

The detailed shapes of extended ^{57}Co and U-metal objects were successfully resolved using the device, demonstrating its potential utility for the black box problem for nuclear security. However, this prototype imager is not easily portable. Its large footprint is mainly the result of a desire for mechanical simplicity rather than any fundamental constraint on size. Since the attractiveness of CdZnTe-based imagers is due in large part to their portability, time modulation should eventually be achieved in a more compact form factor.

ACKNOWLEDGMENT

The authors would like to thank K. Moran of Dream Machine, LLC, for the help in mechanical engineering of the mask positioning system. They would also like to thank J. Berry for providing the engineering support for system testing and those at Y-12 who hosted the authors during their measurement campaign at the Y-12 Nuclear Detection and Sensor Testing Center (NDSTC).

REFERENCES

[1] K. F. Koral, W. L. Rogers, and G. F. Knoll, "Digital tomographic imaging with time-modulated pseudorandom coded aperture and Anger camera," *J. Nucl. Med.*, vol. 16, no. 5, pp. 402–413, May 1975.

[2] W. L. Rogers *et al.*, "Coded-aperture imaging of the heart," *J. Nucl. Med.*, vol. 21, no. 4, pp. 371–378, Apr. 1980.

[3] W. L. Rogers *et al.*, "SPRINT: A stationary detector single photon ring tomograph for brain imaging," *IEEE Trans. Med. Imag.*, vol. MI-1, no. 1, pp. 63–68, Jul. 1982.

[4] M. Oda, "High-resolution X-ray collimator with broad field of view for astronomical use," *Appl. Opt.*, vol. 4, no. 1, p. 143, 1965.

[5] L. Mertz, "A dilute image transform with application to an X-ray star camera," in *Proc. Symp. Mod. Opt.*, 1967, pp. 787–791.

[6] R. H. Dicke, "Scatter-hole cameras for X-rays and gamma rays," *Astrophys. J.*, vol. 153, pp. L101–L106, Aug. 1968.

[7] J. G. Ables, "Fourier transform photography: A new method for X-ray astronomy," *Publications Astronomical Soc. Aust.*, vol. 1, no. 4, pp. 172–173, 1968.

[8] K. F. Koral, J. E. Freitas, W. L. Rogers, and J. W. Keyes, "Thyroid scintigraphy with time-coded aperture," *J. Nucl. Med.*, vol. 20, no. 4, pp. 345–349, Apr. 1979.

[9] G. F. Knoll, W. L. Rogers, K. F. Koral, J. A. Stamos, and N. H. Clinthorne, "Application of coded apertures in tomographic head scanning," *Nucl. Instrum. Methods Phys. Res.*, vol. 221, pp. 226–232, Mar. 1984.

[10] E. E. Fenimore, "Coded aperture imaging: Predicted performance of uniformly redundant arrays," *Appl. Opt.*, vol. 17, no. 22, pp. 3562–3570, 1978.

[11] K. P. Ziock, C. J. Hailey, T. B. Gosnell, J. H. Lupton, and F. A. Harrison, "A gamma-ray imager for arms control," *IEEE Trans. Nucl. Sci.*, vol. 39, no. 4, pp. 1046–1050, Aug. 1992.

[12] K. P. Ziock, N. Madden, E. Hull, W. Craig, T. Lavietes, and C. Cork, "A Germanium-based coded aperture imager," *IEEE Trans. Nucl. Sci.*, vol. 49, no. 4, pp. 1737–1742, Aug. 2002.

[13] P. E. Vanier and L. Forman, "Forming images with thermal neutrons," *Proc. SPIE*, vol. 4784, pp. 183–193, Jan. 2003.

[14] P. A. Hausladen, M. A. Blackston, E. Brubaker, D. L. Chichester, P. Marleau, and R. J. Newby, "Fast-neutron coded-aperture imaging of special nuclear material configurations," Idaho Nat. Lab., Idaho Falls, ID, USA, Tech. Rep. INL/CON-12-26506, Jul. 2012.

[15] K. P. Ziock *et al.*, "Large area imaging detector for long-range, passive detection of fissile material," *IEEE Trans. Nucl. Sci.*, vol. 51, no. 5, pp. 2238–2244, Oct. 2004.

[16] B. R. Kowash, "A rotating modulation imager for the orphan source search problem," Ph.D. dissertation, Univ. Michigan, Ann Arbor, MI, USA, 2008.

[17] P. Marleau *et al.*, "Time encoded fast neutron/gamma imager for large standoff SNM detection," in *Proc. IEEE Nucl. Sci. Symp. Conf. Rec.*, Oct. 2011, pp. 591–595.

[18] J. Brennan, E. Brubaker, A. Nowack, J. Steele, M. Sweany, and D. Throckmorton, "Demonstration of two-dimensional time-encoded imaging of fast neutrons," *Nucl. Instrum. Methods Phys. Res. A, Accel. Spectrom. Detect. Assoc. Equip.*, vol. 802, pp. 76–81, Dec. 2015.

[19] W. Kaye, Y. A. Boucher, F. Zhang, and Z. He, "Calibration and operation of the polaris 18-detector CdZnTe array," in *Proc. IEEE Nucl. Sci. Symp. Med. Imag. Conf.*, Oct./Nov. 2010, pp. 3821–3824.

[20] M. Streicher *et al.*, "A portable 2×2 digital 3D CZT imaging spectrometer system," in *Proc. IEEE Nucl. Sci. Symp. Med. Imag. Conf.*, Nov. 2014, pp. 1–3.

[21] D. Xu, Z. He, C. E. Lehner, and F. Zhang, "4-pi Compton imaging with single 3D position-sensitive CdZnTe detector," *Proc. SPIE*, vol. 5540, pp. 144–155, Oct. 2004.

[22] S. J. Kaye, W. R. Kaye, and Z. He, "Experimental demonstration of coded aperture imaging using thick 3D-position-sensitive CdZnTe detectors," in *Proc. IEEE Nucl. Sci. Symp. Conf. Rec.*, Oct./Nov. 2009, pp. 1902–1906.

[23] S. J. Kaye, W. R. Kaye, J. M. Jaworski, and Z. He, "Experimental limitations of coded aperture imaging using thick 3D-position-sensitive CdZnTe detectors," in *Proc. IEEE Nucl. Sci. Symp. Med. Imag. Conf.*, Oct./Nov. 2010, pp. 3856–3859.

[24] A. E. Bolotnikov *et al.*, "Extended defects in CdZnTe radiation detectors," *IEEE Trans. Nucl. Sci.*, vol. 53, no. 4, pp. 1775–1783, Aug. 2009.

[25] V. Reglero, F. Ballesteros, P. Blay, E. Porras, F. Sánchez, and J. Suso, *Legri Operations. Detectors and Detector Stability*. Dordrecht, The Netherlands: Springer, 2001, pp. 239–253.

[26] Y. A. Boucher, F. Zhang, W. R. Kaye, and Z. He, "Study of long-term CdZnTe stability using the polaris system," *IEEE Trans. Nucl. Sci.*, vol. 60, no. 2, pp. 1086–1093, Apr. 2013.

[27] S. T. Brown, "Time-encoded thermal neutron imaging using large-volume pixelated CdZnTe detectors," Ph.D. dissertation, Univ. Michigan, Ann Arbor, MI, USA, 2017.

[28] E. E. Fenimore and T. M. Cannon, "Coded aperture imaging with uniformly redundant arrays," *Appl. Opt.*, vol. 17, no. 3, pp. 337–347, 1978.

[29] R. D. Byard and D. Ramsden, "Coded aperture imaging using imperfect detector systems," *Nucl. Instrum. Methods Phys. Res. A, Accel. Spectrom. Detect. Assoc. Equip.*, vol. 342, nos. 2–3, pp. 600–608, 1994.

[30] R. Accorsi and R. C. Lanza, "Near-field artifact reduction in planar coded aperture imaging," *Appl. Opt.*, vol. 40, no. 26, pp. 4697–4705, Sep. 2001.

[31] J. E. Grindlay and J. Hong, "Optimizing wide-field coded aperture imaging: Radial mask holes and scanning," *Proc. SPIE*, vol. 5168, pp. 402–410, Jan. 2004.

[32] J. G. M. FitzGerald, L. W. Burggraf, B. R. Kowash, and E. L. Hull, "A modulating liquid collimator for coded aperture adaptive imaging of gamma-rays," *IEEE Trans. Nucl. Sci.*, vol. 60, no. 3, pp. 2300–2307, Jun. 2013.

[33] M. L. McConnell, D. J. Forrest, E. L. Chupp, and P. P. Dunphy, "A coded aperture gamma ray telescope," *IEEE Trans. Nucl. Sci.*, vol. NS-29, no. 1, pp. 155–159, Feb. 1982.

[34] F. Zhang and Z. He, "New readout electronics for 3-D position sensitive CdZnTe/HgI_2 detector arrays," *IEEE Trans. Nucl. Sci.*, vol. 53, no. 5, pp. 3021–3027, Oct. 2006.

[35] K. P. Ziock, M. T. Burks, W. Craig, L. Fabris, E. L. Hull, and N. W. Madden, "Real-time generation of images with pixel-by-pixel spectra for a coded aperture imager with high spectral resolution," *Nucl. Instrum. Methods Phys. Res. A, Accel. Spectrom. Detect. Assoc. Equip.*, vol. 505, nos. 1–2, pp. 420–424, Mar. 2003.